

Cation-Induced Band-Gap Tuning in Organohalide Perovskites: Interplay of Spin–Orbit Coupling and Octahedra Tilting

Anna Amat,[†] Edoardo Mosconi,^{*,†} Enrico Ronca,^{†,‡} Claudio Quarti,[†] Paolo Umari,^{§,||}
Md. K. Nazeeruddin,[†] Michael Grätzel,[†] and Filippo De Angelis^{*,†}

[†]Computational Laboratory for Hybrid/Organic Photovoltaics (CLHYO), CNR-ISTM, Via Elce di Sotto 8, I-06123, Perugia, Italy

[‡]Department of Chemistry, Biochemistry and Biotechnologies, University of Perugia, Via Elce di Sotto 8, I-06123, Perugia, Italy

[§]Dipartimento di Fisica e Astronomia, Università di Padova, via Marzolo 8, I-35131 Padova, Italy

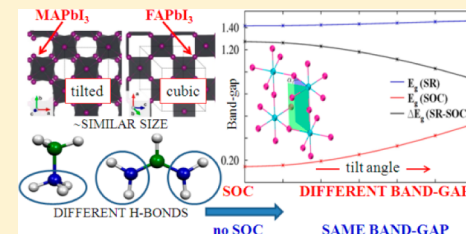
^{||}CNR-IOM DEMOCRITOS, Theory@Elettra Group, c/o Sincrotrone Trieste, Area Science Park, Basovizza, I-34012 Trieste, Italy

[†]Laboratory of Photonics and Interfaces, Institute of Chemical Science and Engineering, EPFL, CH-1015 Lausanne, Switzerland

Supporting Information

ABSTRACT: Organohalide lead perovskites have revolutionized the scenario of emerging photovoltaic technologies. The prototype MAPbI₃ perovskite (MA = CH₃NH₃⁺) has dominated the field, despite only harvesting photons above 750 nm (~1.6 eV). Intensive research efforts are being devoted to find new perovskites with red-shifted absorption onset, along with good charge transport properties. Recently, a new perovskite based on the formamidinium cation ((NH₂)₂CH⁺ = FA) has shown potentially superior properties in terms of band gap and charge transport compared to MAPbI₃. The results have been interpreted in terms of the cation size, with the larger FA cation expectedly delivering reduced band-gaps in Pb-based perovskites. To provide a full understanding of the interplay among size, structure, and organic/inorganic interactions in determining the properties of APbI₃ perovskites, in view of designing new materials and fully exploiting them for solar cells applications, we report a fully first-principles investigation on APbI₃ perovskites with A = Cs⁺, MA, and FA. Our results evidence that the tetragonal-to-quasi cubic structural evolution observed when moving from MA to FA is due to the interplay of size effects and enhanced hydrogen bonding between the FA cations and the inorganic matrix altering the covalent/ionic character of Pb–I bonds. Most notably, the observed cation-induced structural variability promotes markedly different electronic and optical properties in the MAPbI₃ and FAPbI₃ perovskites, mediated by the different spin–orbit coupling, leading to improved charge transport and red-shifted absorption in FAPbI₃ and in general in pseudocubic structures. Our theoretical model constitutes the basis for the rationale design of new and more efficient organohalide perovskites for solar cells applications.

KEYWORDS: Perovskite solar cells, first-principles modeling, spin–orbit coupling, electronic structure



Organohalide lead perovskites have revolutionized the scenario of emerging photovoltaic technologies with recently certified 17.9% efficient solar cells. The prototype CH₃NH₃PbI₃ perovskite (CH₃NH₃⁺ = methylammonium = MA) and the mixed halide MAPb(I_{1-x}Br_x)₃ and MAPb(I_{1-x}Cl_x)₃ analogues have dominated the field.^{1–3} Despite the huge success, these materials are still nonoptimal in terms of optical absorption onset (~1.6 eV). Research is currently focusing on the individuation of new perovskites with red-shifted absorption onset, to improve the light-harvesting efficiency and consequently the short circuit photocurrent density of the related photovoltaic devices. Along with band gap tuning, the perovskite charge transport properties are fundamental ingredients of working devices with efficient electron and hole transport representing a stringent requirement in meso-superstructured/flat heterojunctions and depleted solar cells, respectively.^{4–6}

An intuitive strategy to achieve band gap modulation in the general case of ABX₃ perovskites is to vary the size of A cation,

with larger cations expectedly delivering reduced band-gaps in organohalide perovskites.⁷ The size of the A cation is limited by the Goldschmidt tolerance factor (*t*), which for the case of lead-halide perovskites reads

$$t = \frac{r_A + r_I}{\sqrt{2}(r_{Pb} + r_I)} \quad (1)$$

with *r*_{*i*} being the ionic radii. This relation sets optimal *t* values between 0.9 and 1 for cubic perovskite structures. Considering ionic radii from crystal structures of 2.03 and 1.33 Å for I⁻ and Pb²⁺,⁸ this leaves a range of cation *r*_A values of ~2.3–2.8 Å. Replacement of methylammonium by formamidinium, CH-(NH₂)₂⁺ = FA, Scheme 1, was reported by Stoumpos et al. to effectively lead to a red-shifted absorption onset (~1.5 eV)

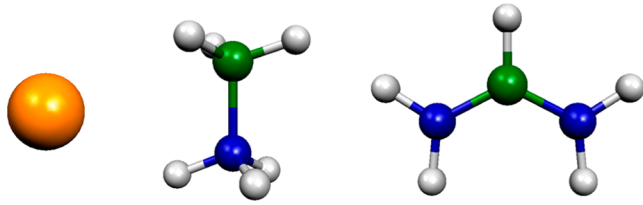
Received: April 8, 2014

Revised: May 2, 2014

Published: May 5, 2014



Scheme 1. Structure of Cs^+ , MA (Methylammonium), and FA (Formamidinium) Cations



compared to MAPbI_3 .⁹ As a matter of fact, solar cells fabricated with FAPbI_3 showed an extended photocurrent generation onset on the red-wing of solar spectrum.^{10–12} Pellet et al.¹² also reported mixed MA-FA perovskites, showing tunable band gap by varying the relative MA/FA amount. On the other hand, a CsPbI_3 perovskite was recently reported by Eperon et al.,^{9,10} showing a blue-shifted absorption onset (1.73 eV), compared to MAPbI_3 , see Supporting Information for UV-vis spectra.

These results have been interpreted in terms of the different cation size, whereby $\text{Cs}^+ < \text{MA} < \text{FA}$, leading to the expected band gap reduction. X-ray diffraction data⁹ showed indeed that the volume per APbI_3 unit is 222, 248, and 256 Å³ for A = Cs^+ , MA and FA, respectively. This data suggests, however, that while there is a large difference between Cs^+ and MA, only a small difference exists between MA and FA. Furthermore, MAPbI_3 crystallizes in the tetragonal $I4/mcm$ (or $I4/cm$) space

group at room temperature, characterized by a sizable tilting of the PbI_6 octahedra,^{9,13} while FAPbI_3 exhibits a trigonal $P3m1$ space group, which as noticed by Pang et al.,¹¹ is close to a cubic structure. The similar volumes per AMX_3 unit exhibited by MAPbI_3 and FAPbI_3 would lend one to think the two materials to exhibit a similar crystal structure, which is however not the case. Thus, one may also wonder whether the different crystal structures (tetragonal versus trigonal/pseudocubic) could play a role, beyond the different volume and/or cation size, in determining the observed variation of optical properties. Finally, the interaction between the organic cations and the inorganic matrix mainly takes place, beyond electrostatics, through hydrogen bonding between the acidic MA or FA hydrogen atoms and the perovskite iodides, which could also contribute to determine the materials properties.

To provide a full understanding of the interplay among size, structure, and organic/inorganic interactions in determining the structural and electronic properties of APbI_3 perovskites, in view of designing new materials and fully exploiting them for solar cells applications, we report here a fully first-principles investigation, based on state-of-the-art DFT and GW methods including spin-orbit coupling (SOC) on APbI_3 perovskites with A = Cs^+ , MA, and FA, including the recently reported mixed organic MA-FA phase.¹² Our results evidence that the tetragonal-to-quasi cubic structural evolution observed when moving from MA to FA is due, beyond the cation size, to

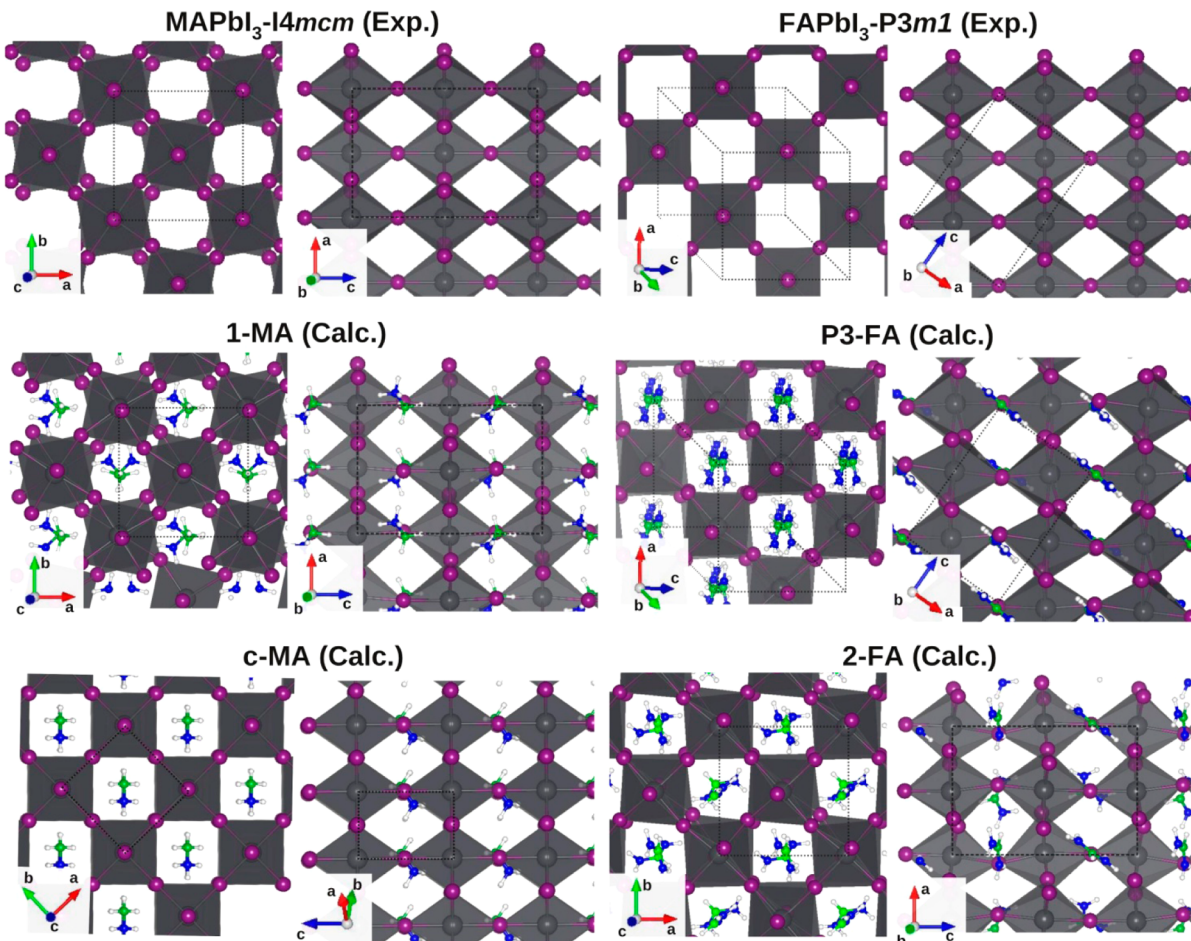


Figure 1. Top: Experimental crystal structure of MAPbI_3 (from ref 13) and of FAPbI_3 (from ref 8). Bottom: Calculated crystal structures of 1-MA, P3-FA, c-MA, and 2-FA, see text for definition. Also shown in all cases are the unit cells. The crystal axes are also shown.

Table 1. ^a

exp. cell parameters ^{14,9}	$a = b = c = 6.33 \text{ \AA}$ Vol = 254		$a = b = 8.86, c = 12.66 \text{ \AA}$ Vol = 248					.
	c-MA	c-FA	1-MA	1-FA ^d	1-MA:FA	2-MA:FA	2-FA	
E_g SR-DFT	1.34	1.31	1.66	1.60	1.59	1.58	1.58	1.63
E_g SOC-DFT	0.11	0.09	0.60	0.55	0.53	0.45	0.46	0.45
ΔE_g DFT	1.23	1.22	1.06	1.05	1.06	1.13	1.12	1.18
E_g SR-GW			2.68				2.65	
E_g SOC-GW			1.67				1.48	
E_g (exp.)			1.6 ^b –1.7 ^c		1.6 ^d		1.5 ^d	
E_{rel} SR	0.053	0.110	0.000		0.006	0.000	0.031	0.000
E_{rel} SOC	0.046	0.110	0.000		0.005	0.000	0.035	0.000
atomic and cell parameters relaxation								
	c-MA	1-MA	1-FA ^d	1-MA:FA	2-MA:FA	2-FA	P3-FA	
E_g SR-DFT	1.30	1.56		1.54	1.54	1.60	1.58	
E_g SOC-DFT	0.07	0.57		0.54	0.42	0.43	0.39	
ΔE_g DFT	1.23	0.99		1.00	1.12	1.17	1.19	
E_{rel} SR	0.062	0.000		0.010	0.000	0.009	0.000	
E_{rel} SOC	0.056	0.000		0.012	0.000	0.011	0.000	
a	6.31	8.78		8.85	8.79	8.84	8.88	
b	6.31	8.76		8.70	8.82	8.85	8.94	
c	6.31	12.70		12.69	12.64	12.54	10.73	
vol	251	244		244	245	245	250	

^aUpper panel: Calculated band-gap (E_g) by SR-DFT, SOC-DFT, and their difference (ΔE_g DFT); SOC-GW band-gap and experimental data; relative energy per APbI_3 unit (eV) (E_{rel} /APbI₃) calculated by SR-DFT and SOC-DFT for the investigated systems employing the experimental cell parameters, also reported along with the volume per APbI_3 unit (Vol, in \AA^3). Bottom panel: Same information for relaxed atomic and cell parameters with calculated structural parameters (\AA). The most stable structure for each type corresponds to zero relative energy. ^bFrom ref 17. ^cFrom ref 18. ^dEstimated from the optical absorption onset in refs 12 and 10.

enhanced hydrogen bonding to the inorganic matrix altering the covalent/ionic character of Pb–I bonds. Most notably, the observed cation-induced structural variability promotes markedly different electronic and optical properties in the MAPbI₃ and FAPbI₃ perovskites, mediated by the different response to SOC. This leads to improved charge transport and red-shifted absorption in FAPbI₃ and in general in pseudocubic structures. Our theoretical model constitutes the basis for the rational design of new and more efficient organohalide perovskites for solar cells applications.

Results and Discussion. We report in Figure 1 a comparison between the experimental tetragonal MAPbI₃¹³ and triclinic FAPbI₃,⁹ and the corresponding structures calculated by scalar-relativistic (SR) DFT, hereafter 1-MA and P3-MA, obtained employing the experimental cell parameters.^{9,14} Similar structures are obtained upon relaxation of atomic coordinates and cell parameters, see Table 1, with calculated cell parameters within 1–2% of the corresponding experimental values. We refer to data obtained employing the experimental cell parameters for facilitating the comparison among the differently investigated structures but an absolutely consistent picture is obtained when referring to fully relaxed (atomic positions and cell parameters) structures, Table 1.

As it can be noticed, in terms of arrangement of the PbI₆ octahedra our calculated structures are generally in good agreement¹⁵ with the experimental crystal structures. The most noticeable difference between MAPbI₃ and FAPbI₃, nicely paralleled in the calculated structures 1-MA and P3-FA, is the sizable out-of-phase octahedra tilting occurring around the c -axis (i.e., in the a/b plane) in MAPbI₃, of $a^0a^0c^-$ type according to the Glazer notation, while both structures are essentially not distorted along the MAPbI₃ tetragonal c -axis and the equivalent FAPbI₃ direction. The calculated 1-MA structure shows an average octahedra tilt angle along the c -axis of 22°, which is in

good agreement with the experimentally measured 21° value by Kawamura et al.¹³ and slightly larger than the 16° value reported by Stoumpos et al.⁹ who, differently from ref 13, suggested an $I4/cm$ space group for MAPbI₃. Notably, our tetragonal structures, calculated without any symmetry constraints, can be assimilated to the ferroelectric $I4/cm$ space group suggested by Stoumpos et al.,⁹ as they are characterized by alternate long–short Pb–I bond lengths along the c axis, see 1-MA in Figure 1. The calculated average alternation of Pb–I bond lengths (3.21 versus 3.16 Å) nicely matches the experimental data (3.20 versus 3.13 Å), showing typical signatures of ferroelectric distortions.⁹

For comparison purposes we also added the cubic MAPbI₃ and FAPbI₃ structures (c-MA, Figure 1, and c-FA, respectively) to the series of calculated structures. We also simulated tetragonal FA structures employing the experimental cell parameters of MAPbI₃. Starting from two different tetragonal structures (1-MA and 2-MA) originated by a different arrangement of the organic cations (head-to-head or head-to-tail), we found 2-FA as the only stable minimum, Figure 1, that is, the starting 1-FA structure converted into 2-FA during the geometry optimization. We thus also considered structure 1-FA*, obtained by optimization of the FA cations inserted into the rigid inorganic 1-MA structure. Notably, structure 2-FA shows a much smaller average octahedra tilt angle along the c -axis compared to 1-MA (7 versus 22°, respectively). In light of the recent study on mixed MA-FA cation perovskites by Pellet et al.,¹² we also simulated a 2:2 MA/FA perovskite employing both the experimental cell parameters of MAPbI₃ and relaxing the cell, see Table 1. In this intermediate case, we could locate both structure of type 1 (1-MA/FA) and 2 (2-MA/FA). The latter is slightly favored (0.02–0.04 eV) over the former and is characterized by a reduced tilt angle around the c -axis (6 versus 21°, respectively). Thus, the different cation (MA or FA) or,

mixed cation systems their ratio, influences the relative stability of the two structural types, characterized by a different tilt angle.

To estimate an operative “ionic radius” for the MA and FA cations, we calculated their volume and that of Cs^+ in the gas phase by DFT, see Method for details, and scaled the resulting radii for the ratio between the calculated radius and experimental ionic radius for Cs^+ (1.81 Å). We obtained values of 2.70 and 2.79 Å for MA and FA, respectively, in keeping with the small difference in the measured crystal volumes. By employing the estimated radii values for MA and FA along with the ionic radii for Pb^{2+} and I^- , we calculate Goldschmidt factors of 0.81, 0.99, and 1.01 for $\text{A} = \text{Cs}^+$, MA, and FA. Clearly, the similar MA and FA size does not account for the different structure of MAPbI_3 and FAPbI_3 . If size is not the only parameter affecting the structural type, thus as we will show below the materials electronic properties, we wondered what could be the determinant factor leading to the observed structural variability.

As previously suggested,¹⁵ structures 1-MA and 2-MA show a different pattern of hydrogen bonding between the acidic MA hydrogens and the perovskite iodine atoms. In search for possible structure/property relations, we thus evaluated the number of H–I hydrogen bonds found within standard bond length/bond angle ranges (2.5–3.5 Å and 0–140°, respectively)¹⁶ for 1-MA, 2-MA, 1-FA*, and 2-FA, finding values of 11, 13, 16, and 18 hydrogen bonds, respectively, see Figure 2.

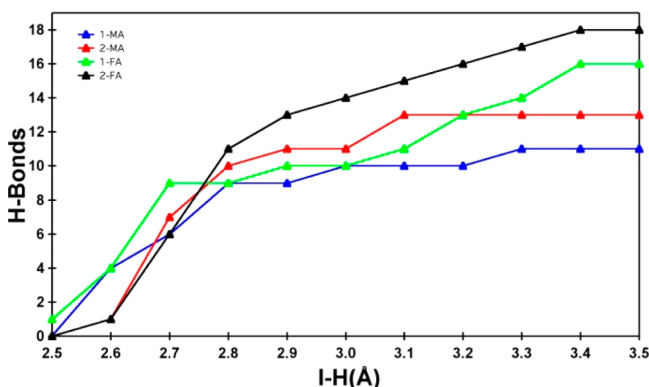


Figure 2. Distribution of hydrogen bonds for structures 1-MA (blue), 2-MA (red), 1-FA* (green), and 2-FA (black).

This analysis confirms our hypothesis, and it also shows that even enforcing the same inorganic part as in 1-MA, cfr. 1-FA*, the FA cation has a higher propensity to form hydrogen bonds. This may be due to the statistically enhanced probability of forming hydrogen bonds by the increased number of FA protons compared to MA (4 versus 3), although MA is possibly a slightly stronger hydrogen bonding donor than FA. As a matter of fact, the ratio of formed hydrogen bonds in structures involving the FA cation is ca. 4/3 that of the corresponding MA cation (e.g., for 2-FA and 2-MA structures the ratio of formed hydrogen bonds 18/13 = 1.38, close to 4/3 = 1.33).

A survey of relevant energetic, structural, and electronic parameters calculated for the different investigated systems at various levels of theory is reported in Table 1.

All the investigated tetragonal systems show a direct band gap at the Γ point of the Brillouin zone, while c-MA/c-FA and P3-FA show a direct band gap at R and A, respectively. As previously found,^{15,19,20} SR-DFT fortuitously (i.e., by cancella-

tion of errors) provides band gap values in good agreement with experiments, while SOC-DFT provides a strong band gap underestimate²¹ which is properly corrected at the SOC-GW level, see Method for computational details.²¹ SOC-DFT, however, qualitatively follows the trend of SOC-GW band-gaps and it can thus be employed for comparative purposes. SOC-GW delivers calculated band-gaps which are within ± 0.1 eV from the corresponding experimental values,²¹ and nicely reproduces the band gap decrease (~ 0.2 eV) observed upon replacing MA with FA. Interestingly, inserting the FA cation into the 1-MA inorganic scaffold, that is, considering structure 1-FA*, also leads to a slight reduction of the calculated band gap compared to 1-MA (1.60/0.55 versus 1.66/0.60 eV by SR-DFT/SOC-DFT, respectively), probably due to the enhanced hydrogen bonding network compared to 1-MA (16 versus 11 hydrogen bonds, see Figure 2).

Most notably, SR-DFT underestimates the MA \rightarrow FA band gap reduction (compare, for example, 1-MA with P3-FA or 2-FA), which is on the other hand captured by SOC-DFT (although underestimating absolute band gap values) and for the considered cases by SOC-GW. A similar behavior is also retrieved by comparing SR- and SOC-GW results, the former delivering only a slight MA \rightarrow FA band gap reduction compared to the latter (0.03 versus 0.20 eV). Also noticeable, is the difference between the band gap calculated by SR- and SOC-DFT which stands at 1.05–1.06 eV for structures of type 1, increasing up to 1.18 eV for P3-FA and to 1.23/1.22 eV for the cubic c-MA and c-FA structures. The same picture holds when referring to optimized atomic and cell parameters. Overall, our data are clearly indicative of a structure-dependent SOC response, which is enhanced for less tilted structures leading to an effective band gap reduction. This is confirmed by looking at c-MA/c-FA, which show the highest band gap variation among the investigated structures. In other words, MAPbI_3 and FAPbI_3 would show essentially the same band gap in the absence of SOC (1.66 versus 1.63 eV for 1-MA and P3-FA, respectively, by SR-DFT and 2.68 versus 2.65 eV by SR-GW). These results also explain why previous calculations performed on cubic MAPbI_3 and FAPbI_3 structures did not show a correct variation of the band gap compared to experiments, irrespective of SOC or the use of hybrid functionals.²² As an illustrative example, due to the calculated structure-dependent SOC response and to the observed structural distortions, the cubic c-MA and tetragonal 1-MA MAPbI_3 structures show a SOC-DFT band gap difference as large as ~ 0.5 eV, see Table 1. As a matter of fact, a quantitative comparison between calculated and experimental band-gaps is only meaningful when considering realistic structural models, related to the phases for which the band gap is measured. Notably, for the mixed cation system, a 2:2 MA/FA ratio is sufficient to (slightly) stabilize structure 2-MA/FA, showing essentially the same octahedra tilting as 2-FA. The predicted structural change is consistent with the observation that similar electrical conductivity properties (activation energy) were found for the pure FAPbI_3 phase and for the $\sim 50:50$ mixed MA/FA perovskite, see below.¹²

To provide a rationale for the observed structure-dependent band gap variation, we resorted to a model tetragonal $[\text{CsPbI}_3]_4$ system, analogous to, for example, 1-MA, and investigated how the SR- and SOC-DFT electronic structure changed as a function of the octahedra tilting, as defined by the α -angle, Figure 3a. This simplified system allows us to lift the effects of the anisotropy of the organic cations, focusing on the inorganic

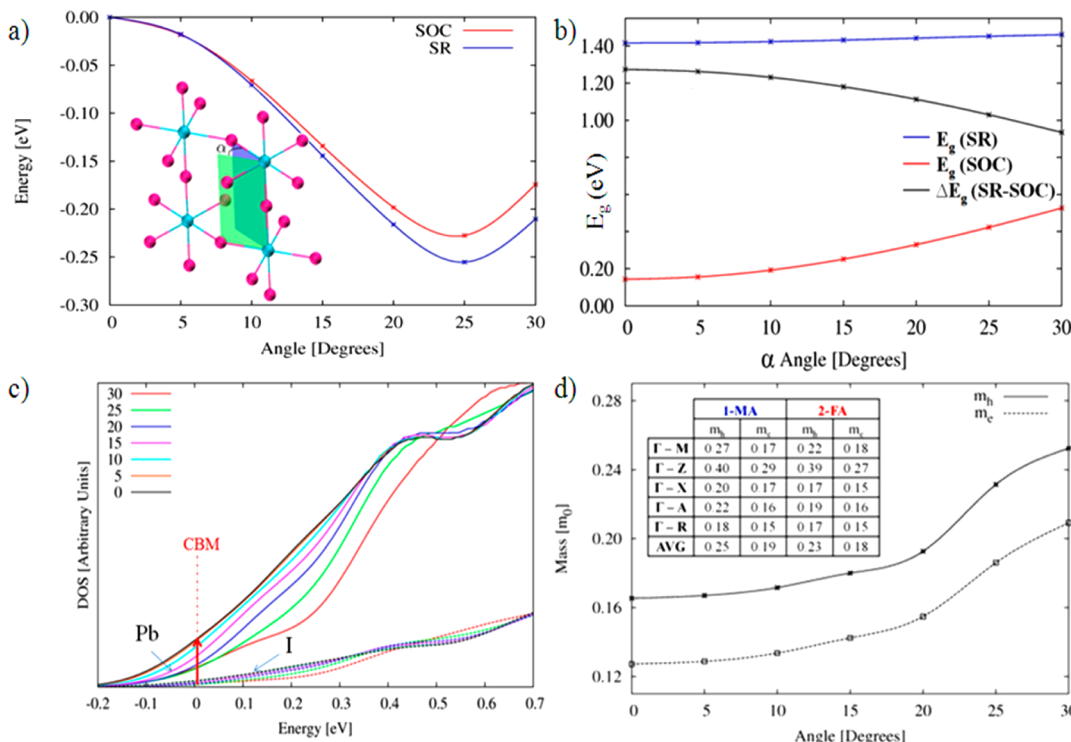


Figure 3. (a) Total energy calculated by SR- and SOC-DFT as a function of the α -dihedral angle, whose definition is shown in the inset. The zero of the energy is set at the energy of $\alpha = 0$. (b) Variation of the calculated band gap (E_g) by SR- and SOC-DFT and their difference (ΔE_g) for the model CsPbI₃ system. (c) Partial lead (solid lines) and iodine (dashed lines) DOS around the conduction band minimum as a function of the varying tilting angle α in the CsPbI₃ system. (d) Variation of the calculated average effective electron (m_e , dashed line) and hole masses (m_h , solid line) by SOC-DFT as a function of α -tilting angle in the CsPbI₃ system. The table in the inset shows the SOC-GW calculated effective masses along the high symmetry directions of the tetragonal Brillouin zone for 1-MA and 2-FA.

lead-iodide structure. We started from a pseudocubic geometry, that is, with $\alpha = 0$ with an optimized Pb–I bond length of 3.23 Å obtained from a separate calculation on a cubic cell, and as α increased we reduced the $a = b$ cell parameters to maintain the same Pb–I bond lengths as in the starting structure without further relaxing the structure (c was maintained at the starting cubic value). This analysis points at a minimum for $\alpha = 25^\circ$, Figure 3a, whose position does not change when the total energy is calculated by SR- or SOC-DFT, despite SOC slightly destabilizes the distorted structures.

The SR- and SOC-DFT band gap variation as a function of α , along with their difference, is plotted in Figure 3b. As it can be noticed, while the SR-DFT calculated band gap only slightly increases with increasing α , the SOC-DFT calculated band gap shows a strong increase, so that their difference (ΔE_g SR-SOC) strongly decreases with α . The calculated SR-GW band-gaps follow the same trend of SR-DFT data, showing essentially the same value (2.6 eV) for $\alpha = 0$ and 25° . This behavior, obtained for the model CsPbI₃ system, actually very nicely reproduces the trend observed for the real structures, Table 1, allowing us to understand the origin of the band gap variation and of the structure-dependent SOC effect in the systems of interest. We thus analyze in Figure 2b the partial density of states (DOS) around the conduction band minimum (CBM) for the CsPbI₃ model calculated by SR-DFT. Notice, it is the SR-DFT data we have to look at because their variation determines the different response to SOC effects. The DOS is decomposed into summed s and p contributions from Pb and I atoms, clearly showing an increase in the Pb character as α decreases from 30 to 0°, that is, passing from a tilted tetragonal to a cubic-like

structure. The increase in Pb character around the CBM readily explains the structure dependent SOC effect manifesting as a different band gap variation in tilted or cubic-like structures. Being that SOC is mainly associated with the heavy Pb centers, an increase of Pb character enhances SOC. The variable amount of Pb character in the DOS with the tilt angle can be associated with the covalency of the Pb–I bonds, which increases upon octahedra tilting,²³ sizably reducing the Pb content up to ~0.5 eV above the CBM. Most notably, the variation of ΔE_g SR-SOC as a function of α provides a perfect ($R^2 = 0.999$) parabolic fitting, Supporting Information, in line with the quadratic behavior expected for a pseudo Jahn–Teller effect, confirming that this effect lies at the heart of octahedra titling in the investigated systems, as proposed by Garcia-Fernandez et al.²³ A similar variation of covalent/ionic character in the Pb-halide bond can be generalized to explain the structural trends observed with different halides, whereby cubic structures are stabilized by mainly ionic bonds in MAPbBr₃ and MAPbCl₃ perovskites, as experimentally found.¹⁴ We recall indeed that the bond covalency increases descending the halide series. In line with this analysis, the increased ionic character of the Pb–I bonds in pseudocubic structures is stabilized by hydrogen bonds to iodine atoms, whose negative partial charge increases upon increasing the ionic character of the Pb–I bond. This explains the structural and electronic diversity of the similarly sized MA- and FA-based perovskites.

Octahedra tilting also leads to substantial changes in the average electron/hole effective masses, calculated by parabolic SOC-DFT band fitting for the model CsPbI₃, and for 1-MA

and 2-FA by SOC-GW, Figure 3d, see Supporting Information for additional data. On the basis of this analysis, the pseudocubic FAPbI₃ perovskite is predicted to be a better electron and hole transporter than the tetragonally distorted MAPbI₃. Notably, this data is also in line with the observed 1-MA/FA → 2-MA/FA structural change, whereby the ~50:50 mixed MA/FA perovskite, which we calculated of pseudocubic type 2, exhibited similar electrical conductivity properties (activation energy) as the pure FAPbI₃ phase, rather than intermediate characteristics between those of MAPbI₃ and FAPbI₃.¹²

Inspection of the total SOC-GW calculated DOS for 1-MA and 2-FA (aligned at the Pb 5d peaks), Figure 4a, reveals sizable

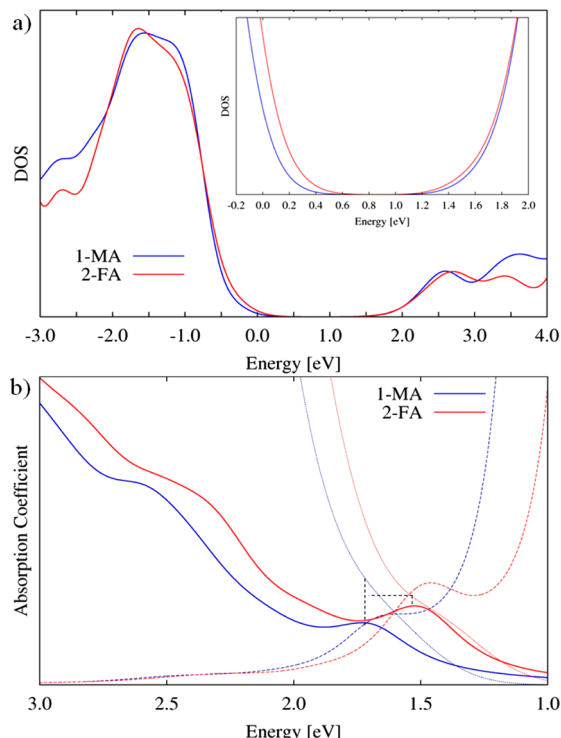


Figure 4. (a) Calculated total density of states (DOS, solid lines) by SOC-GW for 1-MA (blue) and 2-FA (red). Inset: zoom around the CBM/VBM regions. (b) Calculated absorption spectra (solid lines) by SOC-GW for 1-MA (blue) and 2-FA (red). Dotted lines are the SOC-GW calculated joint DOS for 1-MA (blue) and 2-FA (red), while dashed lines represent the ratio between the absorption coefficient and the joint DOS for 1-MA (blue) and 2-FA (red), both in arbitrary but consistent units. Black dashed lines mark the absorption maxima for and the related values of the joint DOS.

differences in the electronic structure of the two materials, both in the valence and conduction band (VB/CB). Our aligned DOS nicely reproduces the subtle energy VB down-shift observed in MAPbI₃ compared to FAPbI₃^{11,24} and suggests a similar CB energy in the two materials, despite a steeper CB/VB rise in MAPbI₃ which is in line with the larger calculated effective masses for this material compared to FAPbI₃. The different electronic structure of the two materials induces sizable differences in the simulated optical absorption spectra (calculated here neglecting electron–hole interactions, see Methods for details) for 1-MA and 2-FA that are reported in Figure 3b. The two spectra are in good agreement with available experimental data, see Supporting Information, although the calculated data is obtained for structure 2-FA

rather than for the experimentally characterized triclinic P3-FA system. 2-FA shows a red-shifted absorption maximum compared to 1-FA, which is in line with the reduced band gap; also, the higher lying spectral feature at 2.6–2.4 eV is red shifted in 2-FA compared to 1-MA and it appears as a less pronounced shoulder in the former.^{10–12} The simulated absorption spectrum of 2-FA is more intense than that of 1-MA throughout the investigated energy range. Thus, for structure 2-FA the spectral red shift is also associated with an intensity increase, which definitely leads to an increased light harvesting for FAPbI₃. To understand the origin of the increased spectral intensity observed for 2-FA, we resort to a Fermi golden rule interpretation of the spectral intensity (although our spectra are calculated from the evaluation of the real and imaginary parts of the frequency dependent dielectric constant, see Method), which for a transition from valence (v) to conduction (c) states reads

$$W_{\vec{k}} \cong \frac{2\pi}{\hbar} |v| |\mathcal{H}'|^2 \delta[E_c(\vec{k}) - E_v(\vec{k}) - \hbar\omega] \quad (2)$$

where for light absorption H' is the dipole operator, and the second part of eq 1 represents a joint density of states.

Having calculated the total absorption coefficient and the joint DOS by SOC-GW, we can thus approximately investigate whether the increased absorption of 2-FA compared to 1-MA is due to a different transition dipole term, or a different joint DOS, or a combination of the two. In Figure 3b, we thus compare the calculated absorption spectra with the joint DOS and with the ratio between the spectral intensity and the joint DOS, which in the Fermi golden rule approximation equals the transition dipole term, cfr eq 2. As it can be noticed, the calculated joint DOS at the absorption maxima for 1-MA is ~10% larger than the what found for 2-FA at its absorption maximum. Surprisingly, our data show that the increased intensity found for 2-FA is thus due to a strongly enhanced transition dipole moment originated by the different electronic structure, as discussed above. Most notably, in absence of SOC effects the opposite holds, see SR-GW data in Supporting Information.

Another interesting property related to SOC is the so-called Rashba/Dresselhaus effect, which shows up as k -dependent band splitting in noncentrosymmetric space groups.²⁰ This effect displaces the VB maximum or CBM away from a symmetry point of the Brillouin zone. The SOC-GW calculated bands for 1-MA and 2-FA are reported in Figure 5 and clearly show a signature of a Rashba/Dresselhaus effect for the CB along the $\Gamma \rightarrow M$ direction, that is, in the plane perpendicular to the c -axis where the alternating long–short Pb–I distances are located, right panel of Figure 5, and to a minor extent along the $\Gamma \rightarrow A/X$ directions. The VB is less affected by SOC due to the dominant iodine contribution though a splitting is still observed. In particular, we can quantify the Rashba/Dresselhaus effect by the parameter defined as $\alpha_R = 2E_R/k_R$ ²⁵ where E_R is the energy difference between the effective CB minimum and the energy at the Γ point, while k_R is the displacement along the considered k -direction. On the basis of the SOC-GW bands, we estimate α_R values of 2.3 and 2.6 eV Å for 1-MA and 2-FA, respectively. These sizable values are a factor ~6 smaller than those reported in GeTe (16 eV Å) for which a “giant Rashba effect” was invoked.²⁵ Notably, 2-FA shows a slightly larger Rashba parameter than 1-MA, in line with the enhanced structure-dependent SOC we found in this model system. The displacement of the CB minimum away

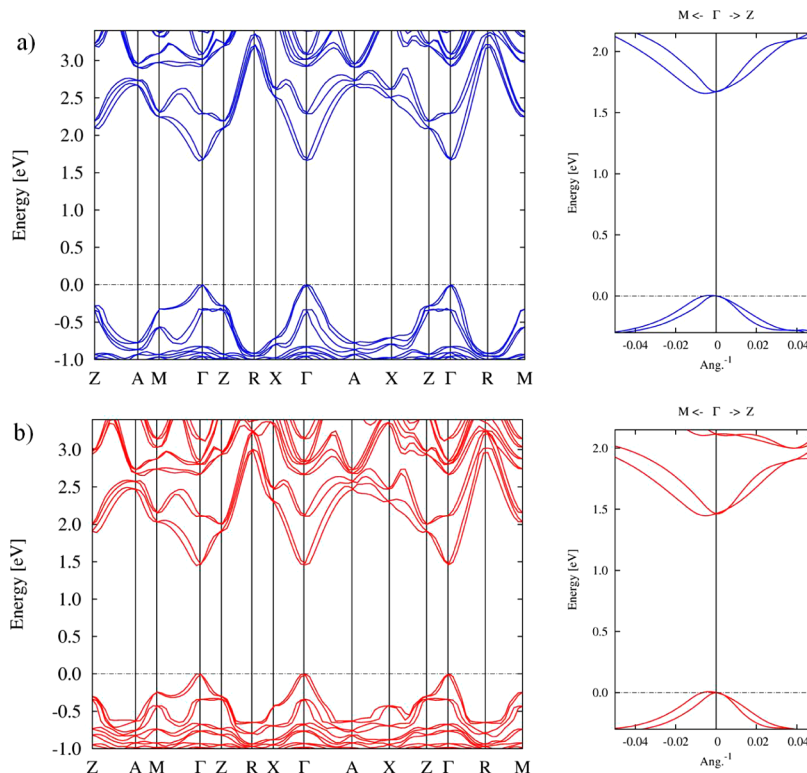


Figure 5. Left: SOC-GW calculated band structure for 1-MA (a, blue lines) and 2-FA (b, red lines) along the high symmetry directions of the tetragonal Brillouin zone Γ (0,0,0) \rightarrow M (0.5, 0.5, 0); $\Gamma \rightarrow Z$ (0,0,0.5); $\Gamma \rightarrow X$ (0,0.5,0); $\Gamma \rightarrow A$ (0.5,0.5,0.5); $\Gamma \rightarrow R$ (0,0.5,0.5). The energy zero is set in both cases at the highest occupied state. Right: Zoom of the band dispersion around Γ .

from Γ could possibly contribute to reduce carrier recombination, thus enhancing the efficiency, of perovskite-based solar cells. Notably, a reduced effect is found for the same tetragonal phase of $MASnI_3$, see calculated SOC-GW bands in Supporting Information, as expected on the basis of the reduced SOC found for Sn compared to Pb.

Conclusions. We have investigated, by state of the art first-principles calculations, the interplay of factors leading to the observed band gap variation observed with different cations in organohalide lead-perovskites for solar cells applications. By considering the experimentally investigated Cs^+ , methylammonium (MA), formamidinium (FA) series of cations, we have assessed how the interplay of different size and hydrogen-bonding properties may influence the structural and electronic properties of $APbI_3$ perovskites. We confirmed that Cs^+ is much smaller than MA, while we found that MA is only slightly smaller than FA, which definitely does not justify the diverse crystal structures (tetragonal versus trigonal/pseudocubic) exhibited by $MAPbI_3$ and $FAPbI_3$. Our analyses point on the other hand at the interplay between size effects and the different statistically higher probability of forming hydrogen bonds of FA compared to MA in stabilizing pseudocubic structures. In turn, pseudocubic structures are found to promote an enhanced spin-orbit coupling compared to octahedrally tilted tetragonal structures (typical of $MAPbI_3$) because of the increased ionic character of Pb–I bonds, which enhances the Pb character in the materials conduction band thus amplifying the effect of spin-orbit coupling. Remarkably, in absence of spin-orbit, the tetragonal $MAPbI_3$ and pseudocubic $FAPbI_3$ would have the same band gap. From a different perspective, including spin-orbit coupling but considering the same cubic structures for MA and FA would

lead to a very similar band gap. Along with the reduced band gap, $FAPbI_3$ is predicted to be a better electron/hole transporter than $MAPbI_3$, thus representing a promising alternative to the prototypical $MAPbI_3$ for even higher photovoltaic performances. We also speculate that the sizable Rashba/Dresselhaus effect observed in the investigated non-centrosymmetric tetragonal structures, originated by spin-orbit coupling, could possibly contribute to reduce carrier recombination in these systems, thus enhancing the efficiency of perovskite-based solar cells.

The demonstrated structure-induced enhancement of spin-orbit coupling, mediated by the interplay of organic cations size and hydrogen bonds, represents the basis for a deeper understanding of the important class of organohalide lead perovskites and may constitute a novel design strategy for new and more efficient materials for solar cells applications.

Method. All the reported calculations have been carried out without any symmetry constraint, using the PWSCF code as implemented in the Quantum-Espresso program package.²⁶ A unit cell consisting of four $APbI_3$ units was used for the tetragonal systems, while for the triclinic P3-FA case the unit cell contained three $FAPbI_3$ units, as experimentally found.⁹ While scalar relativistic (SR) DFT calculations nicely reproduced the structural properties of organohalide lead perovskites,¹⁵ inclusion of spin-orbit coupling (SOC) was found to be mandatory for a correct description of the electronic structure of such systems.^{19,21,27} Electron-ion interactions were described by ultrasoft pseudopotentials²⁸ with electrons from Pb 5d, 6s, 6p; N and C 2s, 2p; H 1s; I 5s, 5p; and Cs 6s shells explicitly included in the calculations. A $4 \times 4 \times 4$ Monkhorst-Pack grid²⁹ was chosen for sampling the Brillouin zone of the tetragonal and triclinic systems, while for

the cubic MAPbI₃ and FAPbI₃, made by a single APbI₃ unit, an 8 × 8 × 8 *k*-point mesh was adopted, consistent with the 4 × 4 × 4 mesh employed for the tetragonal structures. Plane-wave basis set cutoffs for the smooth part of the wave functions and the augmented density of 25 and 200 Ry, respectively, were used. The PBE exchange-correlation functional was employed for all the periodic calculations.³⁰

By following the procedure reported in our previous work,²¹ SR-GW calculations were performed using norm-conserving pseudopotentials with an energy cutoff of 70 Ry defining the plane-waves used for representing the wave functions. GW calculations including SOC²¹ were performed by using ultrasoft²⁸ pseudopotentials and energy cut-offs of 45 and 280 for the wave functions and charge densities, respectively. SR-GW calculations were performed developing polarizability operators on a basis sets obtained as explained in ref³¹ using an energy cutoff of 3 Ry and selecting the 2000 most important basis vectors. The self-energy expectation values are first obtained on imaginary frequency and then analytically continued on the real frequency axis fitting with a two poles expansion.³² SOC-GW calculations were performed including 400 Kohn–Sham states of which the first 200 are doubly occupied.

All the presented GW calculations have been performed sampling the Brillouin's zone at the Gamma point only, although the starting DFT calculations and the long-range parts of the dielectric matrices are evaluated using a regular 4 × 4 × 4 mesh of *k*-points. To calculate the band structures and DOS at the GW level we have envisaged a scheme for introducing GW corrections to DFT energy levels calculated at an arbitrary *k*-point considering only the GW levels calculated at the Γ -point, see ref 21 for further details. For evaluating the optical properties, we have first evaluated the frequency dependent complex dielectric function

$$\epsilon(\omega) = \frac{16\pi}{N_k \Omega} \sum_{k,v,c} \frac{|\phi_{kv}^{\text{rel}}|^2 |\hat{v}| |\phi_{kc}^{\text{rel}}|^2}{(\tilde{E}_{kc}^{\text{GW}} - \tilde{E}_{kv}^{\text{GW}})^2 (\tilde{E}_{kc}^{\text{GW}} - \tilde{E}_{kv}^{\text{GW}} - \omega - i\eta)} \quad (3)$$

where Ω is the volume of the simulation cell, N_k is the total number of *k*-points in the BZ, \hat{v} is the velocity operator, η is an opportune broadening factor, and the indices *v* and *c* run over the occupied and unoccupied states, respectively. The frequency dependent absorption coefficient $\alpha(\omega)$ is then given by

$$\alpha(\omega) = \omega \sqrt{\frac{-\text{Re}\epsilon(\omega) + \sqrt{\text{Re}^2\epsilon(\omega) + \text{Im}^2\epsilon(\omega)}}{2}} \quad (4)$$

To estimate the “ionic radii” of the investigated A cations, we calculated their optimized geometry (for MA and FA) by Gaussian09 (B3LYP/6-31G*), followed by Monte Carlo integration of the volume inside a contour of 0.001 electrons/Bohr³ density, augmented by 0.5 Å, as used in Gaussian09 for constructing effective radii for Onsager solvation models.³³ To compare Cs⁺, MA and FA we performed a single point on the optimized geometries using the LANL2DZ for all atoms and with the corresponding pseudopotential for Cs⁺. For MA and FA LANL2DZ and 6-311++G** basis sets delivered an almost identical ratio of FA/MA radii, 1.034 and 1.036.

ASSOCIATED CONTENT

Supporting Information

Experimental absorption spectra. Optimized geometrical structures. Quadratic fit of the SOC–SR band gap differences as a function of the α dihedral. Effective masses for the CsPbI₃ model. SR-GW data. This material is available free of charge via the Internet at <http://pubs.acs.org>.

AUTHOR INFORMATION

Corresponding Authors

*E-mail: edoardo@thch.unipg.it.

*E-mail: filippo@thch.unipg.it.

Notes

The authors declare no competing financial interest.

ACKNOWLEDGMENTS

The research leading to these results has received funding from the European Union Seventh Framework Programme [FP7/2007–2013] under Grant 604032 of the MESO project. A.A. thanks MIUR-PRIN 2010–2011 Project No. 20104XET32 “DSSCX” for financial support.

REFERENCES

- (1) Burschka, J.; Pellet, N.; Moon, S.-J.; Humphry-Baker, R.; Gao, P.; Nazeeruddin, M. K.; Grätzel, M. *Nature* **2013**, *499*, 316–319.
- (2) Lee, M. M.; Teuscher, J.; Miyasaka, T.; Murakami, T. N.; Snaith, H. J. *Science* **2012**, *338*, 643–647.
- (3) Noh, J. H.; Im, S. H.; Heo, J. H.; Mandal, T. N.; Seok, S. I. *Nano Lett.* **2013**, *13*, 1764–1769.
- (4) Liu, M.; Johnston, M. B.; Snaith, H. J. *Nature* **2013**, *501*, 395–398.
- (5) Docampo, P.; Ball, J. M.; Darwich, M.; Eperon, G. E.; Snaith, H. J. *Nat. Commun.* **2013**, *4*, 2761.
- (6) Laban, W. A.; Etgar, L. *Energy Environ. Sci.* **2013**, *6*, 3249–3253.
- (7) Borriello, I.; Cantele, G.; Ninno, D. *Phys. Rev. B* **2008**, *77*, 235214.
- (8) Shannon, R. D. *Acta Cryst. A* **1976**, *32*, 751–767.
- (9) Stoumpos, C. C.; Malliakas, C. D.; Kanatzidis, M. G. *Inorg. Chem.* **2013**, *52*, 9019–9038.
- (10) Eperon, G. E.; Stranks, S. D.; Menelaou, C.; Johnston, M. B.; Herz, L. M.; Snaith, H. J. *Energy Environ. Sci.* **2014**, *7*, 982–988.
- (11) Pang, S.; Hu, H.; Zhang, J.; Lv, S.; Yu, Y.; Wei, F.; Qin, T.; Xu, H.; Liu, Z.; Cui, G. *Chem. Mater.* **2014**, *26*, 1485–1491.
- (12) Pellet, N.; Gao, P.; Gregori, G.; Yang, T.-Y.; Nazeeruddin, M. K.; Maier, J.; Grätzel, M. *Angew. Chem., Int. Ed.* **2014**, *53*, 3151–3157.
- (13) Kawamura, Y.; Mashiyama, H.; Hasebe, K. *J. Phys. Soc. Jpn.* **2002**, *71*, 1694–1697.
- (14) Poglitsch, A.; Weber, D. *J. Chem. Phys.* **1987**, *87*, 6373–6378.
- (15) Mosconi, E.; Amat, A.; Nazeeruddin, M. K.; Grätzel, M.; De Angelis, F. *J. Phys. Chem. C* **2013**, *117*, 13902–13913.
- (16) Arunan, E.; Desiraju Gautam, R.; Klein Roger, A.; Sadlej, J.; Scheiner, S.; Alkorta, I.; Clary David, C.; Crabtree Robert, H.; Dannenberg Joseph, J.; Hobza, P. *Pure Appl. Chem.* **2011**, *83*, 1637.
- (17) Tanaka, K.; Takahashi, T.; Ban, T.; Kondo, T.; Uchida, K.; Miura, N. *Solid State Commun.* **2003**, *127*, 619–623.
- (18) Schulz, P. E.; Edri, E.; Kirmayer, S.; Hodes, G.; Cahen, D.; Kahn, A. *Energy Environ. Sci.* **2014**, *7*, 1377–1381.
- (19) Even, J.; Pedesseau, L.; Jancu, J.-M.; Katan, C. *J. Phys. Chem. Lett.* **2013**, *4*, 2999–3005.
- (20) Even, J.; Pedesseau, L.; Jancu, J.-M.; Katan, C. *Phys. Status Solidi Rapid Res. Lett.* **2014**, *8*, 31–35.
- (21) Umari, P.; Mosconi, E.; De Angelis, F. *Sci. Rep.* **2014**, *4*, 4467.
- (22) Lang, L.; Yang, J.-H.; Liu, H.-R.; Xiang, H. J.; Gong, X. G. *Phys. Lett. A* **2014**, *378*, 290–293.
- (23) Garcia-Fernandez, P.; Aramburu, J. A.; Barriuso, M. T.; Moreno, M. J. *Phys. Chem. Lett.* **2010**, *1*, 647–651.

- (24) Kim, H.-S.; Lee, C.-R.; Im, J.-H.; Lee, K.-B.; Moehl, T.; Marchioro, A.; Moon, S.-J.; Humphry-Baker, R.; Yum, J.-H.; Moser, J. E.; et al. *Sci. Rep.* **2012**, *2*, 591.
- (25) Di Sante, D.; Barone, P.; Bertacco, R.; Picozzi, S. *Adv. Mater.* **2013**, *25*, 509–513.
- (26) Giannozzi, P.; Baroni, S.; Bonini, N.; Calandra, M.; Car, R.; Cavazzoni, C.; Ceresoli, D.; Guido, L. C.; Cococcioni, M.; Dabo, I.; et al. *J. Phys.: Condens. Matter* **2009**, *21*, 395502.
- (27) Giorgi, G.; Fujisawa, J.-I.; Segawa, H.; Yamashita, K. *J. Phys. Chem. Lett.* **2013**, *4*, 4213–4216.
- (28) Vanderbilt, D. *Phys. Rev. B* **1990**, *41*, 7892–7895.
- (29) Monkhorst, H. J.; Pack, J. D. *Phys. Rev. B* **1976**, *13*, 5188–5192.
- (30) Perdew, J. P.; Burke, K.; Ernzerhof, M. *Phys. Rev. Lett.* **1996**, *77*, 3865–3868.
- (31) Umari, P.; Stenuit, G.; Baroni, S. *Phys. Rev. B* **2010**, *81*, 115104.
- (32) Rieger, M. M.; Steinbeck, L.; White, I. D.; Rojas, H. N.; Godby, R. W. *Comput. Phys. Commun.* **1999**, *117*, 211–228.
- (33) Frisch, M. J.; Trucks, G. W.; Schlegel, H. B.; Scuseria, G. E.; Robb, M. A.; Cheeseman, J. R.; Scalmani, G.; Barone, V.; Mennucci, B.; Petersson, G. A.; Nakatsuji, H.; Caricato, M.; Li, X.; Hratchian, H. P.; Izmaylov, A. F.; Bloino, J.; Zheng, G.; Sonnenberg, J. L.; Hada, M.; Ehara, M.; Toyota, K.; Fukuda, R.; Hasegawa, J.; Ishida, M.; Nakajima, T.; Honda, Y.; Kitao, O.; Nakai, H.; Vreven, T.; Montgomery, J. A., Jr.; Peralta, J. E.; Ogliaro, F.; Bearpark, M.; Heyd, J. J.; Brothers, E.; Kudin, K. N.; Staroverov, V. N.; Kobayashi, R.; Normand, J.; Raghavachari, K.; Rendell, A.; Burant, J. C.; Iyengar, S. S.; Tomasi, J.; Cossi, M.; Rega, N.; Millam, J. M.; Klene, M.; Knox, J. E.; Cross, J. B.; Bakken, V.; Adamo, C.; Jaramillo, J.; Gomperts, R.; Stratmann, R. E.; Yazyev, O.; Austin, A. J.; Cammi, R.; Pomelli, C.; Ochterski, J. W.; Martin, R. L.; Morokuma, K.; Zakrzewski, V. G.; Voth, G. A.; Salvador, P.; Dannenberg, J. J.; Dapprich, S.; Daniels, A. D.; Farkas, O.; Foresman, J. B.; Ortiz, J. V.; Cioslowski, J.; Fox, D. J. *Gaussian 09*; Gaussian, Inc.: Wallingford, CT, 2009.